

Finite element analysis of the mitral apparatus: annulus shape effect and chordal force distribution

V. Prot · R. Haaverstad · B. Skallerud

Received: 28 July 2007 / Accepted: 13 December 2007 / Published online: 10 January 2008
© Springer-Verlag 2008

Abstract This study presents a three-dimensional finite element model of the mitral apparatus using a hyperelastic transversely isotropic material model for the leaflets. The objectives of this study are to illustrate the effects of the annulus shape on the chordal force distribution and on the mitral valve response during systole, to investigate the role of the anterior secondary (strut) chordae and to study the influence of thickness of the leaflets on the leaflets stresses. Hence, analyses are conducted with a moving and fixed saddle shaped annulus and with and without anterior secondary chordae. We found that the tension in the secondary chordae represents 31% of the load carried by the papillary muscles. When removing the anterior secondary chordae, the tension in the primary anterior chordae is almost doubled, the displacement of the anterior leaflet toward the left atrium is also increased. The moving annulus configuration with an increasing annulus saddle height does not give significant changes in the chordal force distribution and in the leaflet stress compared to the fixed annulus. The results also show that the maximum principle stresses in the anterior leaflet are carried by the collagen fibers. The stresses calculated in the leaflets are very sensitive to the thickness employed.

Keywords Mitral valve · Chordal force · Annulus shape · Leaflet stresses · Finite element analysis

1 Introduction

The mitral valve is one of the four valves of the heart, separating the left atrium and the left ventricle. The mitral apparatus consists of an atrioventricular ring or annulus, two leaflets called anterior and posterior, chordae tendinae and two groups of papillary muscles. The anterior leaflet is larger than the posterior leaflet. Both are attached to the mitral annulus and to the chordae tendinae, and the chordae tendinae are attached to the papillary muscles. These muscles are attached to the left ventricular wall. Located between the left atrium and the left ventricle, defects in the mitral apparatus have direct influence on the functionality of the left ventricle, and vice versa. A significant number of people are affected by impairment in both the mitral apparatus and the left ventricle either separately or combined. There is hence a need for a better understanding of the mitral apparatus in order to improve the treatment of mitral valve disease.

During systole the mitral apparatus prevent blood from flowing back into the atrium. Hence, it is of major importance in order to avoid regurgitation.

In order to assess pathologies, one first needs to understand the healthy heart and its tissues. Today the diagnostics obtained using ultrasound have matured to a level showing fine details of tissue motion and blood flow velocities in vivo. It is known that mechanical stress is of primary importance for change and development of the tissue. However, it is not possible to perform stress measurements in vivo. Recently, in vitro studies have been carried out on the mitral apparatus (see [Sacks et al. 2002](#); [Ritchie et al. 2006](#); [Jimenez et al. 2003](#); [Nielsen et al. 1999](#)). These in vitro studies are able to

V. Prot · B. Skallerud (✉)
Department of Structural Engineering, Norwegian University
of Science and Technology, 7491 Trondheim, Norway
e-mail: bjorn.skallerud@ntnu.no

R. Haaverstad
Department of Cardiothoracic Surgery, St. Olav Hospital,
7018 Trondheim, Norway

R. Haaverstad
The Medical Faculty, Norwegian University of Science
and Technology, 7030 Trondheim, Norway

predict the stress state of the chordae and the strain in the leaflets, but not the stress state of the leaflets. With a finite element model it is possible to estimate the stress state of the mitral apparatus. In case of valvular malfunction, surgical repair or replacement of some constituents of the mitral apparatus may be needed. A finite element model can be a tool to study numerically the effects of surgical procedures such as replacement, transection or transposition of chordae by simulating the anatomical changes resulting from surgery or ischemic mitral disease. This can potentially help surgeons to choose the best reconstructive technique. Modeling can also be used to study degenerative diseases affecting the tissues by modifying the material parameters of different parts of the mitral apparatus (Prot et al. 2007a).

In order to predict the stress–strain behavior of the mitral apparatus, one needs to establish proper material models. Previously, numerical simulations of the mitral apparatus have been conducted (see Kunzelman et al. 1993; Votta et al. 2002; Einstein et al. 2004; Dal Pan et al. 2005). In all these finite element studies the annulus was assumed flat and rigid and most employed simplified material models for chordae and leaflets. During the last decade, the material properties of the chordae tendinae and the mitral leaflets have been investigated. (Kunzelman and Cochran 1990; Liao and Vesely 2003), and Ritchie et al. (2006) have performed mechanical tests on different kinds of chordae and highlighted differences in the mechanical behavior depending on size and type of mitral chordae. May-Newman and Yin (1998) conducted biaxial testing for anterior and posterior porcine mitral leaflets.

The geometry of the valve also plays an important role in order to determine the stress state in the leaflets. The mitral annulus shape and its dynamic behavior during the cardiac cycle have been studied in animals and humans using different imaging techniques such as two-dimensional and three-dimensional echocardiography, magnetic resonance etc (see, e.g., Salgo et al. 2002; Tibayan et al. 2003; Green et al. 1999; Flachskampf et al. 2000; Kaplan et al. 2000). Currently, the tendency is to describe the annulus shape as a saddle because of its resemblance to a nonplanar ellipse.

In the present work, an anisotropic material model is used for the valve leaflets based on the mechanical tests of porcine leaflets by May-Newman and Yin (1998). The material model used for the chordae tendinae is based on mechanical tests carried out on porcine chordae by Kunzelman and Cochran (1990). The analyses are based on a recent implementation of a transversely isotropic hyperelastic material model, using the user material interface UMAT in ABAQUS (Prot et al. 2007b). Based on ultrasound measurements and autopsy of the mitral valve in a pig, we established the best possible three dimensional representation of the heart valve geometry for our model. The validity of the finite element model is checked against ultrasound measurements presented herein.

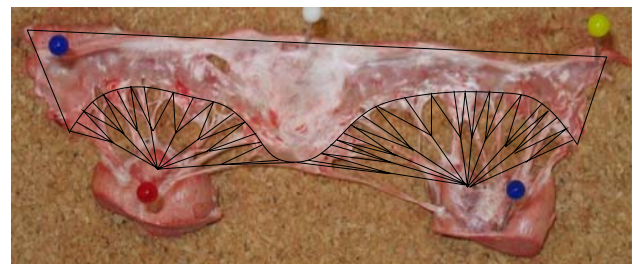


Fig. 1 View of the porcine mitral valve (autopsy picture) and geometric modeling of the chordae and the leaflets

The key points of our study are as follow:

1. As the typical modeling of the annulus is to assume it as flat and rigid whereas we know it has a saddle shape and is nonrigid, the issue of moving or fixed saddle shaped annulus during systole is addressed.
2. The importance of the secondary (strut) chordae on mitral response is investigated by running simulations where they are cut.
3. From the autopsy it is observed that the thickness of the leaflets is inhomogeneous. Herein, we take a very simplistic approach and study the effect on leaflets stress when a homogeneous thickness of 1 or 0.5 mm is employed.

In all above cases, results concerning leaflet stresses, stretches, and chordae force distribution are presented.

2 Methods

2.1 Model geometry, boundary conditions and finite element mesh

In this study, the mitral valve geometry is based on three-dimensional echographic measurements carried out on a pig and on anatomical measurements (see Fig. 1) carried out on the same pig postmortem (at St Olav University Hospital, Trondheim, Norway). The pig used for this study was a Noroc (hybrid of one quarter Duroc, one quarter Yorkshire and one quarter Norwegian landsvin) of 65 kg.

After the pig had been anaesthetized and intubated, the chest was opened. A 3D GE Vingmed ultrasound probe was positioned on the apex. A gel pad was positioned between the probe and the ventricular wall to avoid arrhythmia and improve the resolution of the ultrasound recording. Three-dimensional echocardiography was performed from the apex. Compared to transthoracic echography this technique avoids perturbations due to bones and fat.

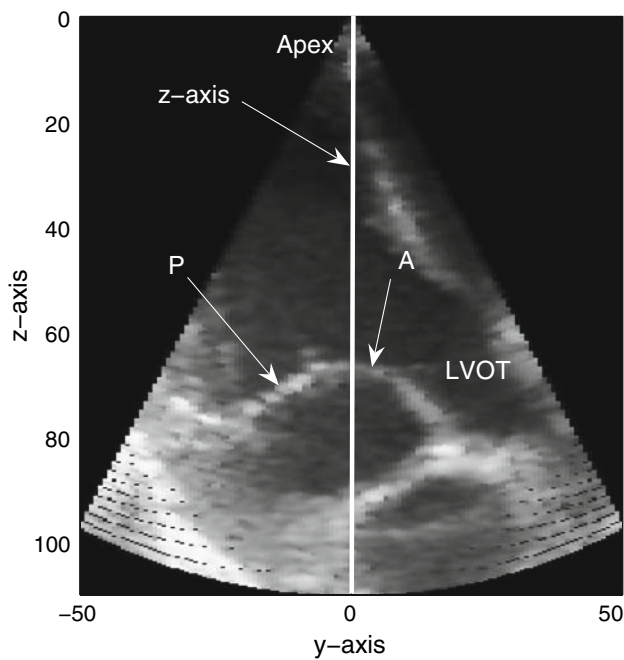


Fig. 2 View of a plane of the 3D ultrasound recording. Anterior (A) and posterior (P) mitral valve leaflets and Left ventricular outflow tract (LVOT)

2.1.1 Annular reconstruction

The three-dimensional shape of the annulus was extracted from the ultrasound recordings with the commercial software Matlab at the beginning of systole and at peak systole. For these time frames, the annulus points were picked manually from the echocardiographic recording.

These 3D points picked along the annulus were transformed into a Cartesian coordinate system with the z -axis aligned with depth-axis of the transducer, see Fig. 2.

In the present study, the shape of the annulus was idealized as a symmetric nonplanar ellipse. The elliptic shape of the annulus was obtained by fitting the ellipse to the x and y coordinates of the points selected along the annulus curve (see Fig. 3). To obtain the nonplanar shape a polynomial fitting (using the Matlab function `polyfit`) was carried out on the x and z coordinates of these points (see Fig. 4). The annulus shape obtained at peak systole is shown in Fig. 5. The dimensions of the idealized annulus are given in Table 1 for beginning and peak systole. The 3D annular perimeter was defined as the path length of the fitted annular curve. The interpeak distance was measured from the highest point of the anterior part of the annulus to the highest point on the opposite side of the annulus, i.e., the posterior part. The posterior part was almost planar during systole and assumed flat in our model. The saddle height was measured as the maximum distance between the anterior annulus and the plane defined the posterior annulus. The interval distance was

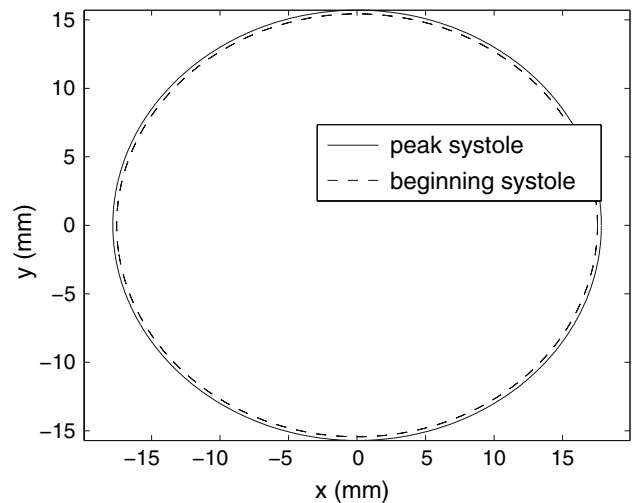


Fig. 3 Planar elliptic shape at beginning of systole (dashed line) and at peak systole (solid line), calculated from 3D ultrasound measurements

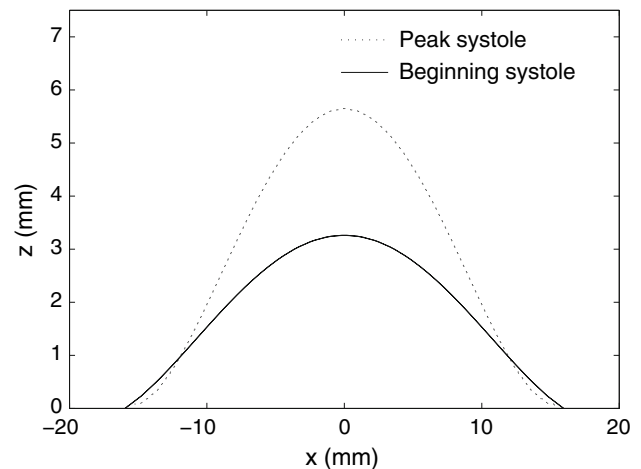


Fig. 4 Polynomial fitting of the x and z coordinates for the anterior part of the mitral annulus at beginning of systole (solid line) and at peak systole (dashed line), calculated from 3D ultrasound measurements

measured between the two lowest points of the annulus, and these points correspond to the commissural part of the valve.

2.1.2 Autopsy measurements

During the autopsy of the pig, the maximum distance from the annulus to the free edge of the anterior and posterior leaflets were measured to be 22 and 11 mm, respectively, and the length of the annulus 105 mm. The annulus length value given by the autopsy agrees well with the one obtained from the 3D reconstruction of the annulus from the echocardiographic data.

The anterior leaflet has a rounded convex free edge and has a larger area than the posterior leaflet. However, the posterior leaflet is narrow and has a longer attachment to the annulus.

Table 1 Dimensions of the idealized annulus

	Saddle height (mm)	Intervalley (mm)	Interpeak (mm)	Perimeter (mm)
Beginning of systole	4.81	34.1	30.9	103.5
Peak systole	6.85	35.6	31.4	108.5

We assumed the posterior leaflet free edge to be divided in three scallops (Ho 2002), a large middle one and two smaller ones representing the commissural parts of the valve.

Figure 1 shows that each papillary muscle is divided in several parts attached to each other. During ventricular contraction, these parts are much closer than shown on the figure (Barlow 1987). Hence, as a modeling simplification, the chordae attached to each of the papillary muscles were assumed to arise from the same point. In addition, the multiple insertions of the marginal chordae to the free edge of the leaflets were modeled with branches arising from the middle point of the marginal chordae (Fig. 1).

The lengths of the chordae were measured to be between 15 and 20 mm. During the autopsy of the pig two types of chordae were observed, the marginal chordae attached to the free edge of the leaflets and the secondary chordae attached beyond the free edge. The cross-section areas of these chordae used in our model were based on the average values given by Liao and Vesely (2003): 0.38 and 2.05 mm² for marginal and secondary chordae, respectively. The secondary chordae considered herein are also called “strut” chordae by Lam et al. (1970) and are observed in 90% of human hearts and are by far the thickest and the largest chordae of the mitral valve. The morphology of the porcine mitral apparatus is close to the human mitral apparatus, hence the presence of these two secondary chordae corresponds to physiological conditions. In total, eight anterior marginal chordae, six posterior marginal chordae, six commissural chordae and two anterior secondary (strut) chordae were attached the leaflets.

2.1.3 Boundary conditions and mesh

The papillary muscles were assumed to be fixed. This assumption is quite consistent with the in vivo finding that the relative distance between the annulus and the papillary muscle tip is nearly constant during systole in normal subjects (Sanfilippo et al. 1992). The leaflets were allowed to rotate at the annular attachment. The chordae were attached at one end to the node representing the papillary muscle and at the other end to a node of the leaflets (a free edge node for the marginal and commissural chordae and a node beyond the free edge for the secondary chordae). A hard contact condition was set between the surfaces of the anterior and posterior leaflets in order to capture coaptation. A finite-sliding and a node to surface formulations were used for the computation

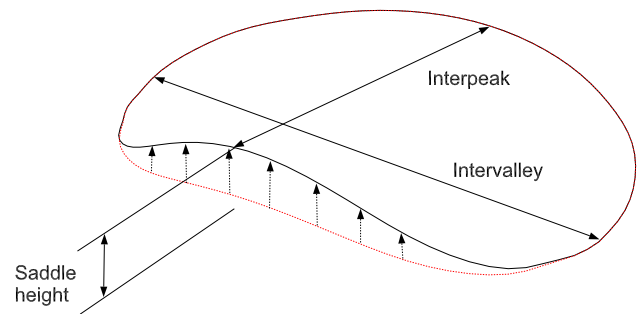


Fig. 5 Three-dimensional shape of the annulus and displacements (arrows) of the anterior annulus during systole (calculated from 3D ultrasound measurements). Undeformed configuration dashed line (position at beginning of systole). Deformed configuration solid line (peak systole)

of the quasi-static analyses (see ABAQUS analysis User's Manual).

Several analyses were conducted with a fixed annulus having the dimensions determined at the beginning of systole and with a moving annulus. In the last case, since the main change in the annulus shape during systole appears to be the increase of the saddle height for the anterior annulus, displacement boundary conditions were prescribed to increase gradually the annulus saddle height from the value determined at the beginning of systole to the one determined at peak systole, see Table 1 and Fig. 5. The ultrasound measurements showed that the posterior part of the annulus did not vary much in shape during systole. Hence, it was kept fixed.

In addition, for both annulus configurations analyses were run with and without secondary chordae to study their influence on the mitral valve response and on the chordal force distribution.

A uniform ventricular pressure was applied on the surface of the leaflets (see Fig. 6).

The peak systolic pressure in the left ventricle measured on the anesthetized pig was 120 mmHg. Additionally, the analyses were conducted with a pressure up to 200 mmHg to study the response at hypertension.

The valve leaflets were meshed with 1090 three noded membrane elements and the chordae with 81 truss elements, see Fig. 7. Note that the figure corresponds to the initial (reference) configuration where the ventricular pressure is zero. Quasi-static conditions were employed in all simulations.

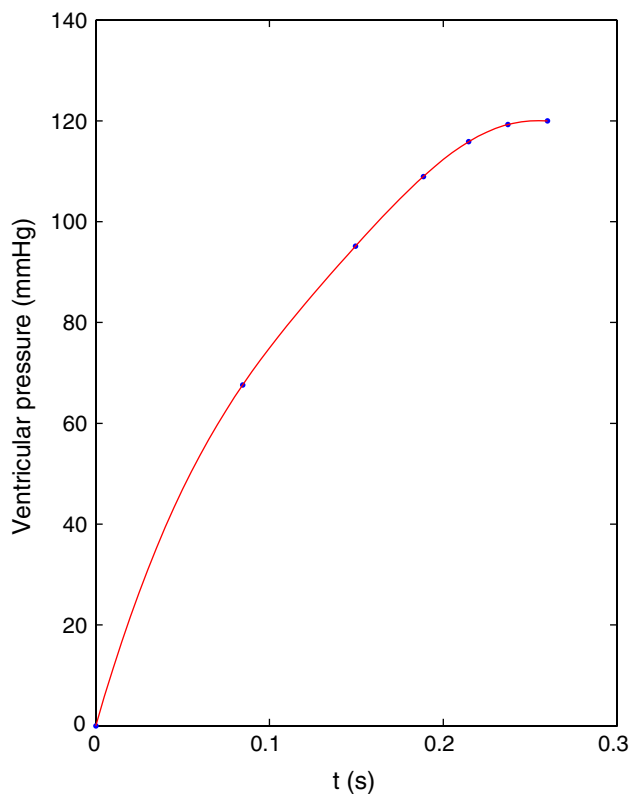


Fig. 6 Left ventricular pressure applied on the ventricular surface of the leaflets from early to peak systole. A quasi-static solution was applied over this period

2.2 Material model

2.2.1 Leaflets

Experimental data provided by [May-Newman and Yin \(1998\)](#) show that the mitral leaflets tissue exhibits highly nonlinear mechanical response and that one approach to derive the material constitutive model of the leaflets can be based on strain invariants and assumption of material incompressibil-

ity and transverse isotropy. The pseudo elastic response was simplified to be hyperelastic.

Here, we recall some continuum mechanics definitions used to derive these constitutive material models.

The deformation gradient is defined as $\mathbf{F} = \partial \mathbf{x} / \partial \mathbf{X}$ where \mathbf{X} is the position of a point in the initial (undeformed) configuration related to a point \mathbf{x} in the current (deformed) configuration. The right Cauchy–Green deformation tensor is denoted $\mathbf{C} = \mathbf{F}^T \mathbf{F}$.

The three invariants of \mathbf{C} given by $I_1 = \text{tr } \mathbf{C}$, $I_2 = 1/2((\text{tr } \mathbf{C})^2 - \text{tr } \mathbf{C}^2)$ and $I_3 = \det \mathbf{C}$ are related to isotropic hyperelasticity.

In order to describe transverse isotropy, the unit vector \mathbf{a}_0 defining the preferred average collagen fiber direction of the material is introduced. It is possible to define two pseudo-invariants I_4 and I_5 of \mathbf{C} and $\mathbf{a}_0 \otimes \mathbf{a}_0$ as $I_4 = \mathbf{a}_0 \cdot \mathbf{C} \mathbf{a}_0$ and $I_5 = \mathbf{a}_0 \cdot \mathbf{C}^2 \mathbf{a}_0$. According to [Spencer \(1984\)](#), the strain energy function of transversely isotropic hyperelasticity can be described by these five invariants.

The stress tensors are derived from a strain energy function Ψ :

$$\mathbf{S} = 2 \frac{\partial \Psi}{\partial \mathbf{C}}, \quad \boldsymbol{\sigma} = J^{-1} \mathbf{F} \mathbf{S} \mathbf{F}^T, \quad (1)$$

where \mathbf{S} and $\boldsymbol{\sigma}$ are the second Piola–Kirchhoff stress tensor and the Cauchy stress tensor, respectively.

The fourth-order material elasticity tensor is determined from:

$$\mathbb{C} = 4 \frac{\partial^2 \Psi}{\partial \mathbf{C}^2}. \quad (2)$$

The strain energy function employed herein to derive the constitutive model is the one proposed by [Holzapfel et al. \(2005\)](#),

$$\Psi(I_1, I_4) = c_0 [\exp^{c_1(I_1-3)^2 + c_2(I_4-1)^2} - 1] + p(J-1), \quad (3)$$

where, c_i , $i = 0, 1, 2$, are material parameters, the scalar p serves as an indeterminate Lagrange multiplier

Fig. 7 Finite element mesh and modeling of the initial configuration of the mitral apparatus

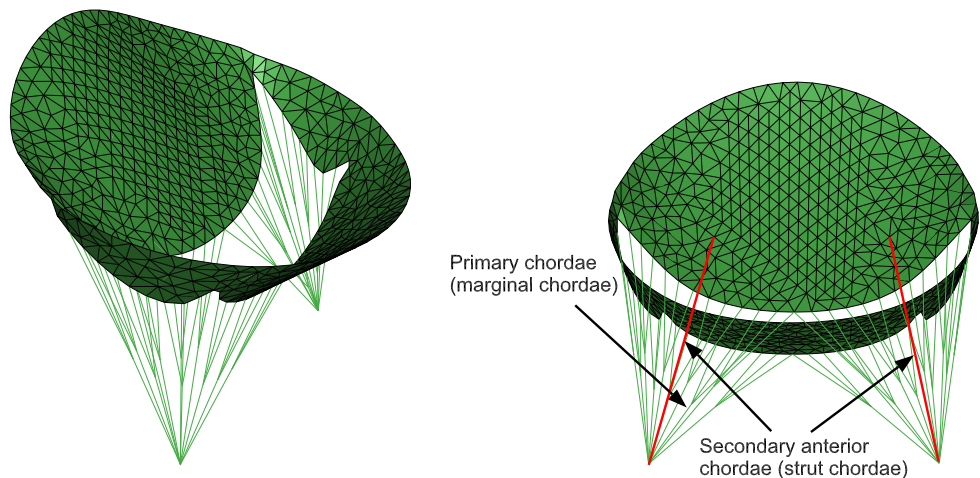


Table 2 Material parameter values for the strain-energy function (3)

	c_0 (kPa)	c_1	c_2
Anterior leaflet	0.0520	4.63	22.6
Posterior leaflet	0.171	5.28	6.46

and $J = \det \mathbf{F}$ is the Jacobian of the deformation. The material parameters c_i , $i = 0, 1, 2$ were fitted to biaxial in vitro tests on porcine mitral valve tissue carried out by [May-Newman and Yin \(1998\)](#), using a nonlinear least square technique. Note that [May-Newman and Yin \(1998\)](#) proposed the following strain energy function, $\Psi(I_1, I_4) = c_0[\exp^{c_1(I_1-3)^2+c_2(\sqrt{I_4}-1)^4} - 1] + p(J - 1)$. The material model derived from this strain energy function was also implemented ([Prot et al. 2007b](#)), but the model derived from (3) showed better numerical efficiency. The anterior and posterior leaflets have different responses, the posterior one is more extensible than the anterior one. The material parameters of the strain energy function (3) are given in Table 2 for both leaflets.

In the present model, the fibers are oriented parallel to the annulus (circumferential direction) in the center of the anterior leaflet, with a gradual transition to an orthogonal orientation (radial direction) at the commissures ([Cochran et al., 1991](#)). [May-Newman and Yin \(1995\)](#) found that the posterior leaflet was stiffer in the circumferential direction (parallel to the annulus) than in the radial direction. As the material model employed herein is based on their study the collagen fibers were oriented parallel to the annulus in the posterior leaflet. But, as shown subsequently, this may not be an optimal collagen orientation. The local collagen direction is set by the material axes, i.e., the local collagen fiber orientation is aligned with the local 1-direction of the membrane elements, see Fig. 8a. The collagen fibers are embedded in the continuum. Their initial orientations are specified

at the start of the analysis and then rotated according to the deformations of the valve leaflets.

2.2.2 Chordae

The chordae were modeled with an incompressible isotropic hyperelastic material. The nonlinear stress-stretch behaviour was implemented from experimental data published by [Kunzelman and Cochran \(1990\)](#). The same material model was used for all the chordae derived from the following strain energy function,

$$U(I_1) = a_1(\exp^{a_2(I_1-1)} - 1), \quad (4)$$

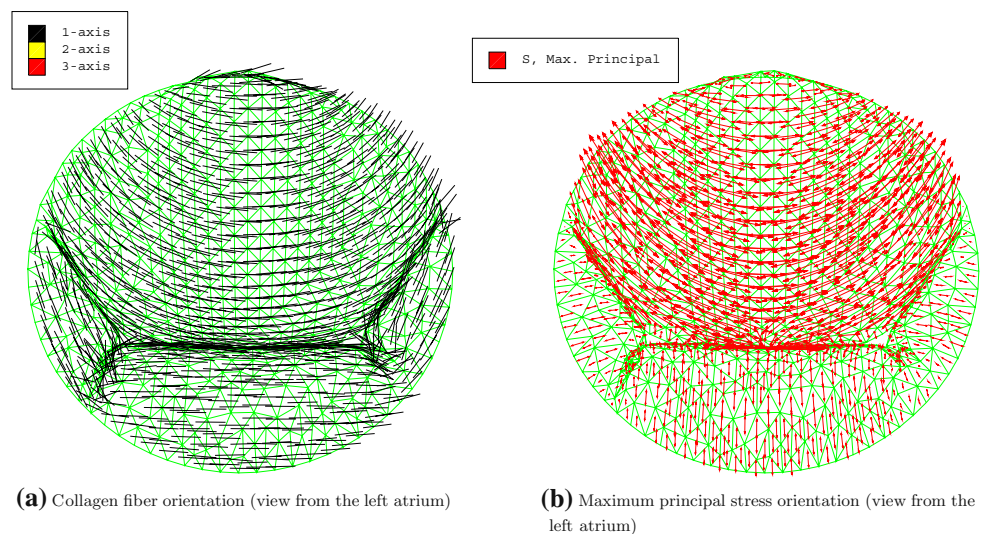
$a_1 = 0.0565$ kPa and $a_2 = 29.6$ for the marginal chordae and $a_1 = 0.050$ kPa and $a_2 = 35$ for the secondary chordae (strut chordae).

3 Results

3.1 Leaflet stresses

The collagen fiber orientation and the maximum principal stress orientation are plotted in Fig. 8 at a systolic pressure of 120 mmHg. In the anterior leaflet, the fiber direction and the maximum principal stress direction are nearly aligned, this is not the case in the posterior leaflet where the principal stresses are nearly perpendicular the collagen fiber direction. This nonphysiological result is addressed in Sect. 4. The directions of the highest maximum principal stresses flow from the fibrous trigones to the secondary chordae insertion zone. The stresses are higher in the anterior leaflet than in the posterior leaflet. The Von Mises stresses are plotted on the valve leaflets at a systolic pressure of 120 mmHg in Fig. 9 for two different leaflet thicknesses: 0.5 and 1 mm. The

Fig. 8 **a** The collagen fiber orientation plotted at a systolic pressure of 120 mmHg, **b** the maximal principal stress orientation in the leaflets plotted at a systolic pressure of 120 mmHg (FE calculation)



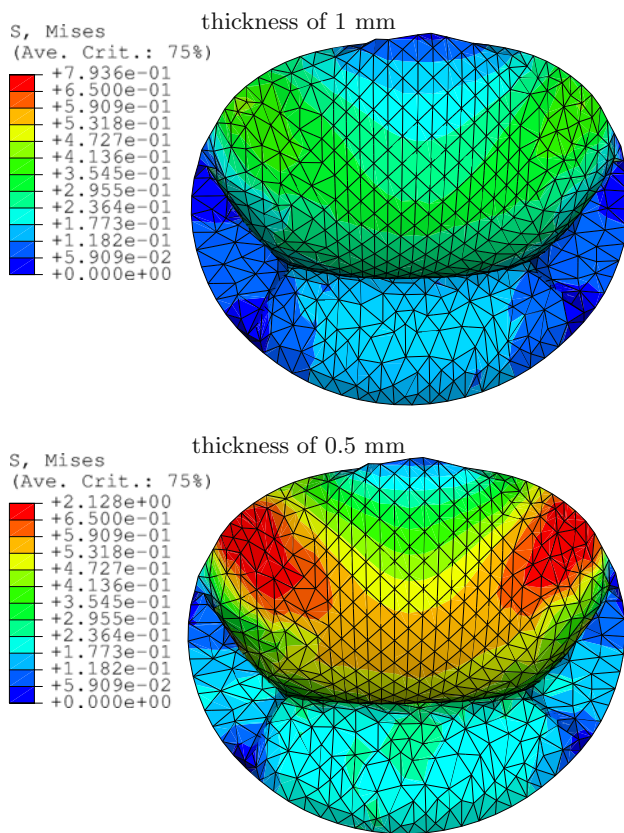


Fig. 9 FE calculation of Von Mises stresses plotted at a systolic pressure of 120 mmHg (MPa) for simulations using 0.5 and 1 mm for the thickness of the leaflets (without strut chordae)

maximum Von Mises stresses were approximately two times higher with a thickness of 0.5 mm than with a thickness of 1 mm.

3.2 Anterior leaflet stretches

In Fig. 10 the principal stretches in a central region of interest of the anterior leaflet are plotted against the ventricular pressure, for different leaflet thicknesses: 0.5 and 1 mm. These results are compared to the maximum measured stretches from the in vitro study by Sacks et al. (2002).

In this region, the collagen fibers are oriented parallel to the annulus (i.e. parallel to the circumferential direction), which means that the local 1-direction of the membrane surface is parallel to the annulus. The minor direction of the principal stretch (λ_1) was aligned parallel to the fibers and the major direction of the principal stretch (λ_2) was aligned perpendicularly to the fibers. As Sacks et al. (2002), who measured the surface strains in in vitro tests on porcine mitral leaflets, we observe a rapid increase in the principal stretches during the closure of the valve and after the ventricular pressure reaches a value of 40 mmHg the principal stretches values are nearly constant. λ_2 was 1.19 times greater than λ_1

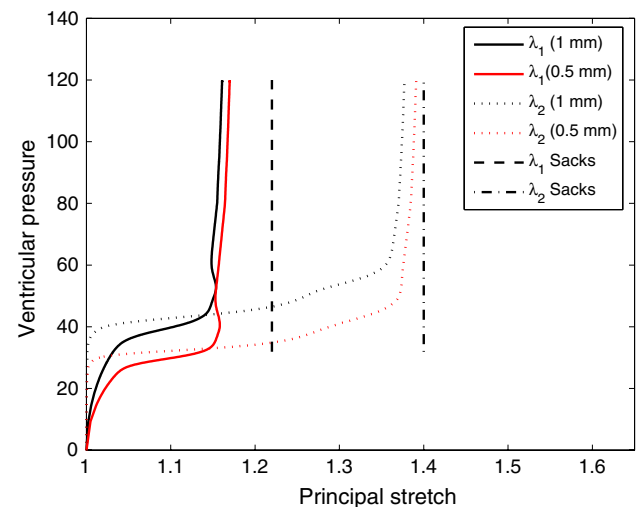


Fig. 10 Principal stretches in the central region of the anterior leaflet for two different thicknesses obtained from FE calculation. The results are compared to the principal stretch values obtained experimentally by Sacks et al. (2002) after the closure of the valve

at a pressure of 120 mmHg. The value of λ_2 at a systolic pressure of 120 mmHg is very similar to the one obtained by Sacks et al. (2002) but our model gives a somewhat stiffer behavior along the fibers. The values obtained at a pressure of 120 mmHg for the principal stretches using a leaflet thickness of 0.5 mm were 1.03 and 1.01 times greater than with a leaflet thickness of 1 mm in the directions parallel and perpendicular to the fiber, respectively. In addition, we observe that the coaptation of the leaflets occurs at 30 mmHg with the simulation using 0.5 mm for the thickness of the leaflet and at 40 mmHg with a thickness of 1 mm.

3.3 Chordae tensions and stretches

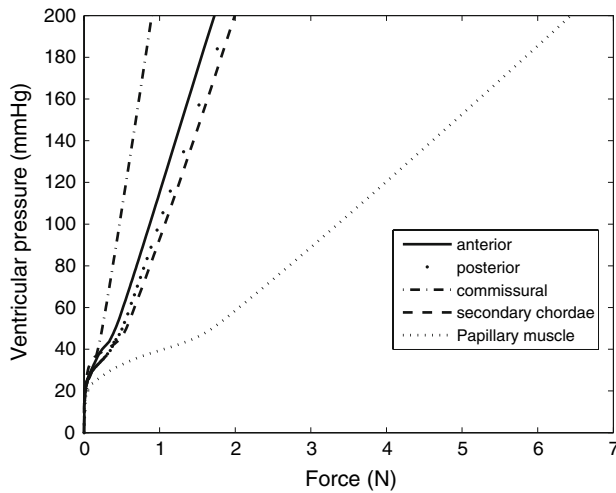
Analyses were carried out with a fixed saddle annulus and a moving saddle annulus, respectively. In both cases two analyses were performed, a first one with two secondary chordae attached on the anterior leaflet (healthy case) and a second one without secondary chordae (pathological case).

The forces carried by the different chordae at a systolic pressure of 120 mmHg are given in Table 3 for both annulus models, with and without secondary chordae.

The tensions reported in Table 3 are slightly higher in the anterior marginal chordae for the fixed annulus, however the moving annulus and the fixed annulus does not induce any significant differences in force distribution in the chordae. Table 3 shows that the tension in the anterior marginal chordae is 1.7 times higher when the secondary chordae are removed. In addition, the tension in the secondary chordae is at least three times higher than in any other chordae.

Table 3 Summary of chordae tendinae tension at a systolic pressure of 120 mmHg

Chordae	Number	With secondary chordae				No secondary chordae			
		Moving annulus		Fixed annulus		Moving annulus		Fixed annulus	
		F (N)	SD	F (N)	SD	F (N)	SD	F (N)	SD
Anterior marginal	4	0.27	0.13	0.28	0.13	0.46	0.18	0.46	0.19
Posterior marginal	3	0.40	0.069	0.40	0.069	0.43	0.084	0.42	0.056
Commissural	3	0.19	0.056	0.19	0.056	0.19	0.056	0.19	0.083
Anterior secondary chordae	1	1.3	—	1.3	—	—	—	—	—

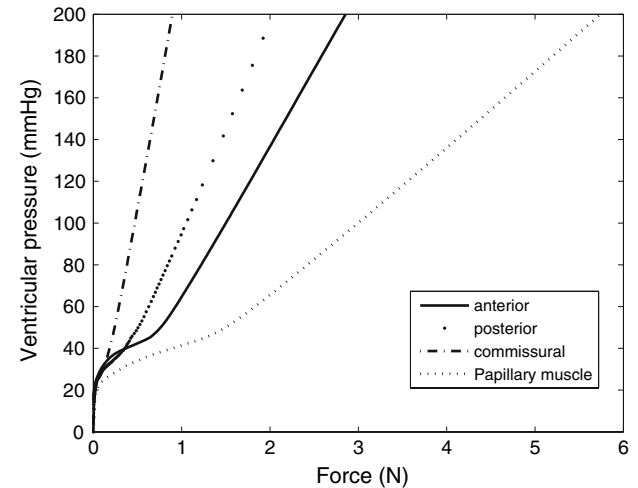
**Fig. 11** Forces carried by the different groups of chordae and the papillary muscle to which they are attached in the simulation using a moving annulus and secondary chordae (FE calculation)

The tensions in the different chordae obtained from the analyses are of the same magnitude as the ones obtained by Jimenez et al. (2003) from experiments carried out in vitro on human mitral apparatus.

In Figs. 11 and 12, the forces carried by the different groups of chordae and the corresponding papillary muscle are plotted against ventricular pressure for the simulations with and without secondary chordae, using a moving annulus.

At a systolic pressure of 120 mmHg the forces carried by the posterior marginal, anterior marginal and anterior secondary chordae are almost equal. However, when the anterior secondary chordae are removed the forces carried by the anterior marginal chordae group is multiplied by 1.64.

The percentages of the force carried by the different groups of chordae relative to the total papillary muscle force are given in Table 4. If we call \mathbf{R} the force vector carried by the papillary muscle, \mathbf{R} is equal to the sum of the vectors representing the tension in each chordae attached to this papillary muscle. Hence, if the force carried by one group of chordae is represented by the vector \mathbf{T} the proportion of \mathbf{R} carried by this group was calculated as,

**Fig. 12** Forces carried by the different groups of chordae and the papillary muscle to which they are attached in the simulation using a moving annulus without secondary chordae (FE calculation)

$$\frac{\|\mathbf{R}\| - \|\mathbf{R} - \mathbf{T}\|}{\|\mathbf{R}\|}$$

When the secondary chordae are removed the proportion of the load carried by the group of anterior marginal chordae increases from 29 to 50%. The simulations with the secondary chordae shows an even distribution of the load between the anterior marginal, posterior marginal chordae groups and the secondary chordae.

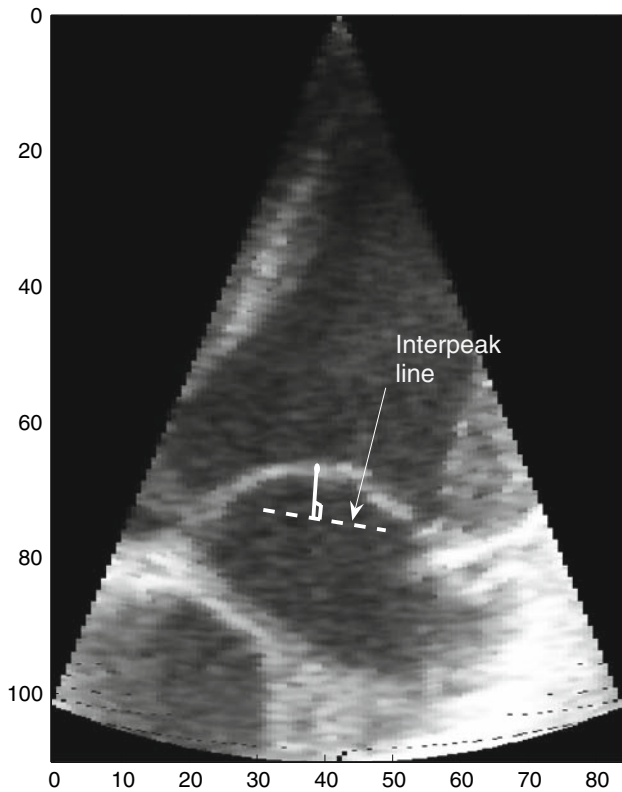
Using the moving or the fixed annulus, the stretches in the chordae remained nearly unchanged and were equal to 1.05, 1.07, 1.04 and 1.05 at a systolic pressure of 120 mmHg, in the anterior marginal, posterior marginal, commissural and strut chordae, respectively.

3.4 Ultrasound comparison

In this section, the global finite element model response is compared with two-dimensional ultrasound measurements carried out on the pig. The relative displacement Δ_{rel} toward the interpeak line (see Fig. 13) of a node located in the

Table 4 Distribution of the force carried by one papillary muscle among the different groups of chordae at a systolic pressure of 120 mmHg for the simulation using a flexible annulus, with and without secondary chordae

Chordae groups	With secondary chordae (%)	No secondary chordae (%)
Anterior marginal	26	50
Posterior marginal	29	35
Commissural	14	15
Anterior secondary chordae	31	–

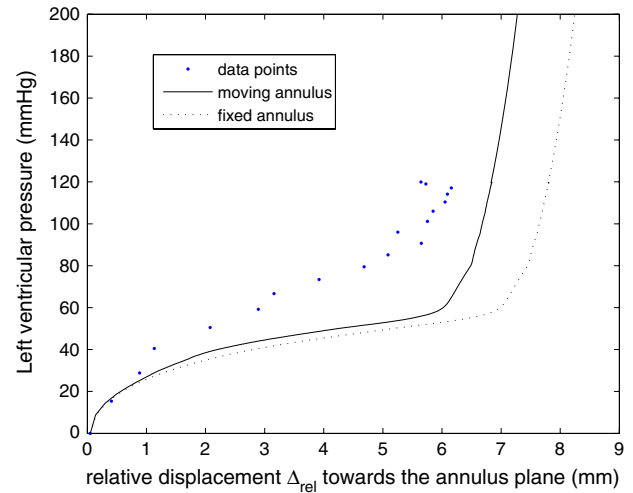
**Fig. 13** 2D ultrasound data. The *dashed line* represents the interpeak line between the two annulus points. The *solid line* is the measured relative displacement Δ_{rel} of the anterior mitral leaflet with respect to the annulus plane

middle of the anterior leaflet is compared with the echographic measurements.

The displacement of the node is compared to the 2D ultrasound measurements in Fig. 14 for different configurations: fixed saddle shaped annulus with secondary chordae and moving saddle shaped annulus with secondary chordae. The configuration with the moving annulus shows the best agreement with the ultrasound data.

Δ_{rel} is given in Table 5 for the different configurations and the 2D ultrasound measurements at a systolic pressure of 120 mmHg.

With the moving annulus, Δ_{rel} is 0.8 mm larger when the secondary chordae are removed.

**Fig. 14** Comparison of the displacement toward the interpeak line of a node located in the middle of the anterior leaflet

3.5 Hypertension

In this section, the results obtained with a systolic pressure of 200 mmHg are compared to those obtained at 120 mmHg (i.e., the ventricular pressure measured on the anaesthetized pig). The tensions in the different groups of chordae are related in Table 6 for this pressure level.

The force carried by one papillary muscle at systolic pressure values of 120 mmHg and 200 mmHg for the flexible annulus configuration (with secondary chordae) was 3.97 and 6.42 N, respectively. The relative displacement toward the interpeak line Δ_{rel} of the same node used in Fig. 14 at systolic pressure values of 120 and 200 mmHg for the flexible annulus configuration (with secondary chordae) was 6.8 and 7.2 mm, respectively.

4 Discussion

A three-dimensional finite element model has been developed to assess the mitral valve response. A hyperelastic transversely isotropic material model was used to account for the different constituents and fiber direction in the mitral valve.

Table 5 Summary of the relative displacement Δ_{rel} towards the interpeak line at a systolic pressure of 120 mmHg

	With secondary chordae		No secondary chordae		Ultrasound
	Moving annulus	Fixed annulus	Moving annulus	Fixed annulus	
$\Delta_{rel}(\text{mm})$	6.8	7.7	7.6	8.5	≈ 6

Table 6 Summary of chordae tendinae tension at a systolic pressure of 200 mmHg

Chordae	Number	With secondary chordae				No secondary chordae			
		Moving annulus		Fixed annulus		Moving annulus		Fixed annulus	
		F (N)	SD	F (N)	SD	F (N)	SD	F (N)	SD
Anterior marginal	4	0.44	0.22	0.46	0.23	0.73	0.31	0.75	0.32
Posterior marginal	3	0.64	0.11	0.64	0.11	0.69	0.14	0.69	0.14
Commissural	3	0.30	0.093	0.30	0.095	0.30	0.094	0.30	0.094
Anterior secondary chordae	1	2.0	–	2.0	–	–	–	–	–

The results obtained for the chordal force distribution from our finite element analysis are in good agreement with the results of the in vitro study of [Jimenez et al. \(2003\)](#). This indicates that the branches adopted in the modeling of the chordae tendinae (see Fig. 1) is a suitable choice.

The tension in a single secondary chordae is higher than the load carried by any of the other groups composed of three or four marginal chordae (see Fig. 1) and represents 29% of the total load carried by the papillary muscle. This shows their importance in the structure of the mitral apparatus. This result is in agreement with the study conducted by [Sedrandsk et al. \(2002\)](#) where anterior secondary chordae exhibit much higher failure load than the other types of chordae and may explain why the secondary chordae are larger than the marginal ones.

In Table 4, we observe that when the secondary chordae are present, the load carried by the marginal anterior and posterior chordae groups are almost equal. The analyses in which anterior secondary chordae are removed show a significant increase of the tension in the anterior marginal chordae (see Table 3). Hence, cut or failure of the secondary chordae may lead to deterioration or even failure of other chordae remaining due to higher loading.

Contrary to the study conducted by [Jimenez et al. \(2003\)](#), the flexible annulus configuration with an increasing annulus saddle height does not give significant changes in the chordal force distribution. However, [Jimenez et al. \(2003\)](#) compared the results between two rigid annulus shape configurations having a saddle height difference of 9 mm while in the present work the saddle height is increased by 2 mm only. Mitral annulus saddle shape varies from species to species, but the anatomy of the porcine mitral valve is quite close

to the human one. Thus the increase of 2 mm of the saddle height that was prescribed in this study between beginning of systole and peak systole is in good agreement with the results given by [Kaplan et al. \(2000\)](#).

Our simulations show that the anterior secondary chordae reduce the motion of the anterior leaflet toward the left atrium. However, when they are removed, we find that the marginal chordae alone are sufficient to insure the proper closure of the valve and prevent mitral valve prolapse. In mitral valve surgery, the practical importance of this is the employment of multiple and strong artificial chordae attached to the free edge in treatment of anterior leaflet prolapse.

In Table 7, the Von Mises stresses obtained with fixed saddle and moving saddle annulus configurations are compared to those obtained with existing flat annulus finite element models at a similar pressure level (120 mmHg) and with similar geometries. The maximum Von Mises stresses obtained with the fixed saddle shape configurations show a quite good agreement with those obtained by [Dal Pan et al. \(2005\)](#) with a hyperelastic isotropic model. A hyperelastic isotropic material model may be sufficient to determine the Mises equivalent stress level in the leaflets, but in order to determine principal stresses, the inclusion of the collagen fibers in the material model is important.

The stresses in posterior leaflet were found to be lower than in the anterior leaflet (Fig. 9), as the posterior leaflet is smaller and carry less load. In the anterior leaflet, the maximum stresses were observed close to the fibrous trigones along the annulus. These areas are located where the annulus has the highest curvature. The study conducted by [Salgo et al. \(2002\)](#) using a linear elastic material model for the leaflets and fixed boundary conditions for the annulus and

Table 7 Comparison of maximum Von Mises stress with other existing FEM models

Maximum Von Mises stress (MPa)	Systole (120 mmHg)	Thickness (mm)
Moving annulus	0.386	1
Anterior leaflet	0.243	1
Posterior leaflet		
Fixed annulus	0.371	1
Anterior leaflet	0.243	1
Posterior leaflet		
<i>Hyperelastic isotropic model results</i>		
Dal Pan et al. (2005)	0.330	–
Anterior leaflet	0.252	–
Posterior leaflet		
<i>Linear-elastic model results</i>		
Dal Pan et al. (2005)	0.336	–
Anterior leaflet	0.225	–
Posterior leaflet		
Kunzelman et al. (1993)	0.350	1.31
Anterior leaflet	0.200	1.26
Posterior leaflet		
Votta et al. (2002)	0.396	0.8
Anterior leaflet	0.194	0.8
Posterior leaflet		

the chordae showed that the leaflet stresses were reduced when the saddle height was increased. However, the present work does not give any significant differences in the anterior leaflet stresses when increasing the annulus saddle height in the physiological regime of the pig employed herein.

The directions of the maximum principal stresses in the anterior leaflet are nearly aligned with the collagen fiber orientation. This result shows that the maximum principal stresses are carried by the collagen fibers in the anterior leaflet. According to the results of May-Newman and Yin (1995), the collagen fibers in the posterior leaflet are oriented parallel to the annulus in our model. In the posterior leaflet, the calculated maximum principal stress direction were nearly orthogonal to the collagen fibers. This does not seem physiological and it would be logic that the fibers will orient according to the maximum principal stress direction. Hence, an analysis with the collagen fibers orthogonal to the annulus in the posterior leaflet was performed and gave the same principal stress directions. Note that this latter collagen fiber orientation for the posterior leaflet did not affect the chordae load distribution. This may indicate that our collagen fiber orientation in the posterior leaflet shown in Fig. 8a, is not correct. This warrants further study.

The peak pressure in the left ventricle measured on the anaesthetized pig was 120 mmHg. Our simulations show that the stresses in the mitral apparatus increase significantly if the peak systolic pressure is increased. On the other hand, the global motions and the strains of the mitral apparatus are

not very sensitive to the pressure level after complete closure of the valve. This is due to the typical soft tissue stress–strain exponential behavior of the its different constituents. Before closure the chordae and the leaflets are soft enough to allow proper coaptation of the mitral valve. After closure, the chordae tendinae and the leaflets become stiffer and prevent further deformations of the valve.

The thickness of the leaflets is also an important aspect in the modeling of the mitral apparatus. In the rough zone, the anterior leaflet is thicker, the width of this zone is about one third of the anterior leaflet length. However, the thickness of the leaflet can be much lower in the area with no chordal attachment. Our simulations show that the closure of the valve and the stress level in the leaflets strongly depends on thickness: the stresses are much greater and the closure of the valve happens at a lower pressure value with thinner leaflets. However, coaptation should occur for even lower pressure value. This deviation may be due to the starting position of the valve in our simulation. This delay in the closure of the valve was also observed with the finite element model using shell elements of Lim et al. (2005). In their study, the valve was still open during IVC (isovolumetric contraction) and achieved complete closure at the end of IVC, i.e., at approximatively 40 mmHg.

The present work agrees with Sacks et al. (2002) in that the leaflets undergo large anisotropic stretches during closure. Although, the use of an isotropic material model for the leaflet may give a good prediction of the average stress level

in the leaflets, our results shows that it is not appropriate for a study of principal strains and stresses.

5 Conclusion

The current analyses point out the importance of the anterior secondary chordae on the mitral systolic function manifested by the chordal force distribution and the apical displacement of the anterior leaflet.

The annulus flexibility introduced in this study, i.e., increase of the saddle height, does not seem to modify much the chordal force distribution or the stress distribution of the leaflets.

The stresses in the mitral apparatus appear to be sensitive to the pressure level during the whole systole whereas the deformations remain nearly constant after complete coaptation of the leaflets.

The stresses calculated in the leaflets are very sensitive to the thickness employed. This points out the importance of the evaluation of the thickness for the stress calculation in the leaflets.

6 Limitations

In the present work, the mitral valve was assumed to be symmetric and only the variation of the saddle height was prescribed as boundary conditions for the flexible annulus. According to Kaplan et al. (2000), the annulus area, the inter-peak distance and the intervalley distance decrease rapidly between beginning and mid-systole and at the same time the height of the saddle shape increases. The mitral valve function may depend on all these variations of the annular shape and area. In future studies, these changes of the annulus will be included as boundary conditions to get a better understanding of their influence on the mitral valve response and on the mitral apparatus stresses. Although the displacements of the papillary muscles may have an important role in the mitral valve dynamics, they were not accounted for in the present model due to the difficulty to determine them from the ultrasound measurements.

More data on leaflet thickness and collagen fiber orientation (for the posterior leaflet in particular) are also needed in order to be more accurate in the modeling of the leaflets.

The material model used for the leaflets is based on mechanical data from the central region of the anterior and posterior leaflets. As no data currently exists for other regions of the leaflet, these experimental data were used to model the whole leaflets. This is most likely too simplistic and motivates for further tests of constitutive behavior.

As membrane elements are used in this study, the stress distribution in the leaflets must be considered with care. The

regions of high membrane stress are predicted. But, the use of solid elements to model the valve leaflets is more accurate in order to account for the variation of stress and deformation through the thickness, see Prot (2008).

The present finite element model does not account for the effect of the fluid on the valve. However, the hemodynamics in the left ventricle and its interaction with the mitral valve is highly relevant in order to understand the global function of the heart. Hence, a fluid structure interaction model including the left ventricular wall is necessary to investigate the interaction between the mitral valve dynamics, the blood flow and the left ventricle.

Acknowledgments The authors are grateful to the following persons for helpful discussions and assistance, associate professor Ivar Nordrum (Department of Laboratory Medicine, Children's and Women's Health, NTNU, Norway), MD Hans Henrik Dedichen (Department of circulation and medical imaging, NTNU, Norway), MD Håvard Bersås Nordgaard (Department of Cardiothoracic Surgery, St. Olav Hospital, Norway), professor Hans Torp (Department of circulation and medical imaging, NTNU, Norway), Dr. Lasse Løvestakken (Department of circulation and medical imaging, NTNU, Norway) and Mr. Bjarne Bergheim (Department of circulation and medical imaging, NTNU, Norway).

References

- Barlow JB (1987) Perspectives on the mitral valve. F.A. Davis, Philadelphia
- Cochran RP, Kunzelman KS, Chuong CJ, Sacks MS, Eberhart RC (1991) Nondestructive analysis of mitral valve collagen fiber orientation. *ASIAO Trans* 37(3):447–448
- Dal Pan F, Donzella G, Fucci C, Schreiber M (2005) Structural effects of an innovative surgical technique to repair heart valve defects. *J Biomech* 38:2460–2471
- Einstein DR, Kunzelman KS, Reinhal P, Nicosia M, Cochran RP (2004) Haemodynamic determinants of the mitral valve closure sound: a finite element study. *Med Biol Eng Comput* 42:832–846
- Flachskampf FA, Chandra S, Gaddipatti A, Levine RA, Weyman AE, Ameling W, Hanrath P, Thomas JD (2000) Analysis of shape and motion of the mitral annulus in subjects with and without cardiomyopathy by echocardiographic 3-dimensional reconstruction. *J Am Soc Echocardiogr* 13(4):277–87
- Green GR, Dagum P, Glasson JR, Daughters GT, Bolger AF, Foppiano LE, Berry GJ, Ingels NB Jr, Miller DC (1999) Mitral annular dilatation and papillary muscle dislocation without mitral regurgitation in sheep. *Circulation* 100:95–102
- Ho SY (2002) Anatomy of the mitral valve. *Heart* 88:5–10
- Holzappel GA, Sommer G, Gasser CT, Regitnig P (2005) Determination of the layer-specific mechanical properties of human coronary arteries with non-atherosclerotic intimal thickening, and related constitutive modelling. *Am J Physiol Heart Circ Physiol* 289:H2048–2058
- Jimenez JH, Soerensen DD, He Z, He S, Yoganathan AP (2003) Effects of a Saddle Shaped Annulus on Mitral Valve Function and Chordal Force Distribution: An In Vitro Study. *Annals of Biomedical Engineering* 31:1171–1181
- Kaplan SR, Bashein G, Sheehan FH, Legget ME, Munt B, Li X-N, Sivarajan M, Bolson EL, Zeppa M, Martin RW (2000) Three-dimensional echocardiographic assessment of annular shape changes in the normal and regurgitant mitral valve. *American Heart Journal* 139:378–87

- Kunzelman KS, Cochran RP (1990) Mechanical properties of basal and marginal mitral valve chordae tendineae. *ASAIO Trans* 36:M405–408
- Kunzelman KS, Cochran RP, Chuong C, Ring WS, Verrier ED, Eberhart RD (1993) Finite element analysis of the mitral valve. *J Heart Valve Dis* 2:326–340
- Lam JH, Ranganathan N, Wigle ED, Silver MD (1970) Morphology of the human mitral valve: I. Chordae tendinae: a new classification. *Circ* 41:449–458
- Liao J, Vesely I (2003) A structural basis for the size-related mechanical properties of mitral valve chordae tendineae. *J Biomech* 36(8):1125–33
- Lim KH, Yeo JH, Duran CM (2005) Three-dimensional asymmetrical modeling of the mitral valve: a finite element study with dynamic boundaries. *J Heart Valve Dis* 14:386–392
- May-Newman K, Yin FCP (1995) Biaxial mechanical behavior of excised porcine mitral valve. *J Biomech Eng* 120:38–47
- May-Newman K, Yin FCP (1998) A constitutive law for mitral valve tissue. *Am J Physiol* 269:1319–1327
- Nielsen SL, Nygaard H, Fontaine AA, Hasenkam JM, He S, Andersen NT, Yoganathan AP (1999) Chordal force distribution determines systolic mitral leaflet configuration and severity of functional mitral regurgitation - design of a new surgical approach for ventricular remodeling to relieve ischemic mitral regurgitation. *Journal of the American College of Cardiology* 33:843–853
- Prot V, Skallerud B, Holzapfel GA (2007a) Effects of connective tissue pathologies on mitral valve response. *MHM 2007, Modelling of heterogeneous materials with applications in construction and biomedical engineering*, Prague 106–107
- Prot V, Skallerud B, Holzapfel GA (2007b) Transversely isotropic membrane shells with application to mitral valve mechanics. *Constitutive modeling and finite element implementation. International Journal for Numerical Methods in Engineering* 71(8):987–1008
- Prot V (2008) Numerical modelling of the mitral apparatus (PhD thesis). Trondheim, Norway. Norwegian University of Science and Technology
- Ritchie J, Jimenez J, He Z, Sacks MS, Yoganathan AP (2006) The material properties of the native porcine mitral valve chordae tendineae: an in vitro investigation. *J Biomech* 39(6):1129–35
- Sacks MS, He Z, Baijens L, Wanant S, Shah P, Sugimoto H, Yoganathan AP (2002) Surface Strains in the Anterior Leaflet of the Functioning Mitral Valve. *Annals of Biomedical Engineering* 30:1281–1290
- Salgo IS, Gorman JH, Gorman RC, Jackson BM, Bowen FW, Plappert T, StJohn Sutton MG, Edmunds LH Jr (2002) Effect of annular shape on leaflet curvature in reducing mitral leaflet stress. *Circulation* 106(6):711–7
- Sanfilippo AJ, Harrigan P, Popovic AD, Weyman AE, Levine RA (1992) Papillary muscle traction in mitral valve prolapse: quantitation by two-dimensional echocardiography. *J Am Coll Cardiol* 19:564–571
- Sedrandsk L, Grande-Allen KJ, Vesely I (2002) Failure mechanics of mitral valve chordae tendinae. *Journal of Heart Valve Disease* 11:644–650
- Spencer AJM (1984) Constitutive theory for strongly anisotropic solids. In: Spencer AJM (ed) *Continuum Theory of the Mechanics of Fibre-Reinforced Composites*, pages 1–32. Springer-Verlag, Wien. CISM Courses and Lectures No. 282, International Centre for Mechanical Sciences
- Tibayan FA, Rodriguez F, Zasio MK, Bailey L, Liang D, Daughters GT, Langer F, Ingels NB Jr, Miller DC (2003) Geometric Distortions of the Mitral Valvular-Ventricular Complex in Chronic Ischemic Mitral Regurgitation. *Circulation* 108:116–121
- Votta E, Maisano F, Soncini M, Redaelli A, Montecocchi FM, Alfieri O (2002) 3-D computational analysis of the stress distribution on the leaflets after edge-to-edge repair of mitral regurgitation. *J Heart Valve Dis* 11:810–822